Light Yield Nonuniformity in PWO Scintillators

Author: María Marteinsdóttir

Supervisor: Per-Erik Tegnér

November 6, 2009

Abstract

In this master thesis, nonuniformity measurements of the light yield for eleven scintillation crystals of different shapes were done. The crystals were made of lead tungstate, $PbWO_4$, and will be located in the barrel part of the electromagnetic calorimeter of the PANDA detector. The PANDA detector is a detector system at FAIR, a new accelerator facility for nuclear physics research, and is under construction at GSI, Germany.

The measured light yield was not uniform, i.e. the light yield depends on the location in the crystal of the energy deposition. The variation of the light yield along the crystal dependents on the tapering angles of the crystals. Larger angles give a larger variation in the result.

Simulation to mimic the PANDA calorimeter was done, to find out how the nonuniformity of the light yield affects the energy resolution. This is compared to contributions from energy leakage from the detector and to Poisson statistics of the light collection process. For the most tapered crystals the nonuniformity of the light yield has a major influence on the energy resolution for energies between 50 MeV and 7000 MeV. For lower energies the Poisson statistics influences the resolution the most. At the highest energies, the energy leakage has the largest contribution.

Contents

1 Introduction

A new accelerator facility for nuclear physics research is under construction at GSI, Gesellschaft für Schwerionenforschung, located outside of Darmstadt in Germany. The facility is called FAIR, which stands for Facility for Antiproton and Ion Research. The PANDA detector (anti-Proton ANhiliation at DArmstadt) is a detector system at FAIR, focused on understanding the nature of strong interaction and of hadronic matter. An important part of the PANDA detector is the electromagnetic calorimeter, (EMC). Its purpose is to identify photons over a wide energy range, from a few tens of MeV up to several GeV [1].

The EMC detector consists of three parts, a barrel part, a forward end cap and a backward end cap. Each part is filled with crystals of different shapes, made of lead tungstate, $PbWO_4$, in the following denoted by PWO. When a high-energy photon hits the crystals in the EMC detector, it produces a signal which contains information on the energy and the position of the incident photon. The detector therefore must be able to give good energy, position and timing resolution over this wide energy range [1].

Various factors can impair the energy resolution of the detector. One is the nonuniformity of the light collection in the scintillator material, PWO. Uniformity means that the light yield from the crystal is independent on the interaction point of the photon. However, that is seldom the case and therefore it is important to measure this fluctuation in light yield since it translates to a fluctuation in the signal amplitude and thereby affects the energy resolution.

In this thesis, eleven crystals of different shapes, located in the barrel part of the EMC, are investigated. These crystals have a tapered shape which may lead to variation in light yield. The question to be answered is if this nonuniformity so large that it has to be compensated for.

The structure of the thesis is as follows. In Chapter 2, the properties of the EMC detector will be introduced. Chapter 3 describes the main physics processes involved when a matter is irradiated with γ-ray photons. In chapter 4, light yield measurements of the scintillation crystals are presented. The instrumentation and the fundamental properties of the PWO crystals are also described and the energy resolution of a scintillator detector is defined. Chapter 5 discusses simulations with the program Geant4 where energy depth deposition is calculated for γ-ray radiation with different initial energies. Finally, chapter 6 presents how the energy resolution is affected due to the nonuniformity as well as energy leakage and Poisson statistics.

2 The Electromagnetic Calorimeter of the PANDA Detector

The PANDA detector is an international collaboration consisting of more than 420 collaborators from 55 institutions in 17 countries. The first experiments are scheduled around year 2015. The electromagnetic calorimeter, inside the PANDA detector, consists of a barrel part, filled with 11360 crystals, a forward end cap with 3600 crystals and a backward end cap with 592 crystals. The total number of crystals is thus 15552. It is proposed that the crystals will have length of 20 cm, and a front end face of approximately 2cm x 2cm but with different tapering.

Experiments in the PANDA detector will be performed using a cooled antiproton beam with a momentum between 1.5 GeV/c and 15 GeV/c, which interacts with an internal target, either a hydrogen cluster jet or a high frequency frozen hydrogen pellet target [1]. The interaction will be at a crosspoint located inside a large superconducting solenoid, which provides a field strength of 2T. The electromagnetic calorimeter, EMC, will be inside this solenoid, see figure 2.1. It will achieve a geometrical coverage of almost 4π. The read-out in the barrel and the backward end cap of the EMC will most likely be done using Avalanche Photo Diodes, while recently developed vacuum photo triodes (VPT) will be used for the forward end cap [2].

As outlined in the introduction, the scintillator material for the EMC detector will be lead tungstate, PWO. This material is chosen due to its fast response and high density. The drawback is the small light yield [1]. Since the detector is suppose to be capable of identify very low energy photons, the light yield of the detectors has to be maximized. To increase the light output by a factor of 4, the crystals are cooled down to -25°C [1].

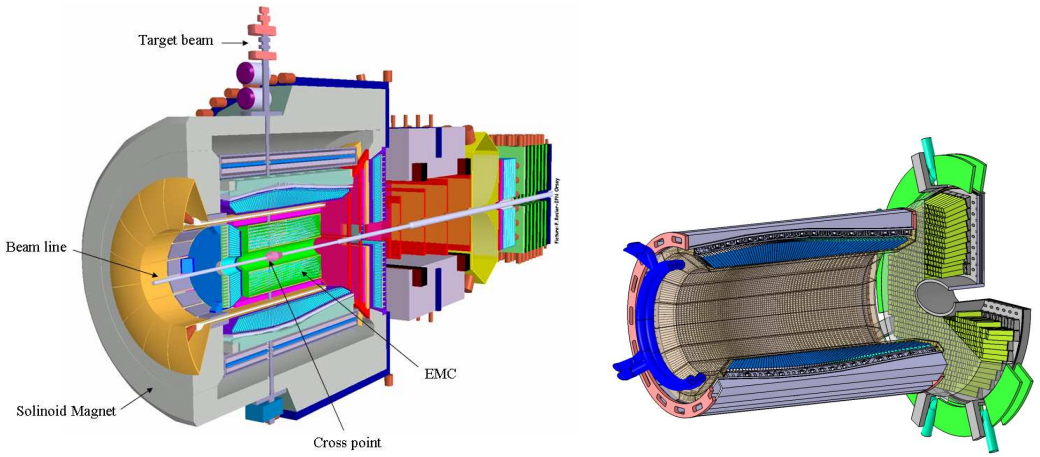

(a) (b)

Figure 2.1: (a) The PANDA detector. The electromagnetic calorimeter, EMC, is marked. The length of PANDA is around 12 m. From [3]. (b) The barrel and the forward end cap of the EMC. The structure of the crystals can be seen. The EMC is around 4 m long. From [4].

3 Particle Interactions in Matter

3.1 Interaction of γ-ray Photons

The three main interactions of γ-ray photons in matter are *photoelectric effect*, *Compton scattering* and *pair production*. Figure 3.1 shows the relative importance of these processes.

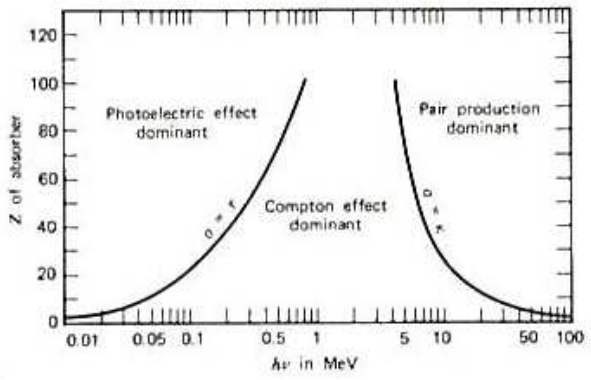

Figure 3.1: Relative importance for the three interaction processes for gamma-rays. From [5]. Pair production is the dominant interaction at PANDA.

As a γ-ray photon beam passes through a matter of thickness t, the intensity of the original beam attenuates according to

$$I = I_0 e^{-\mu t} \tag{3.1}$$

where I_0 is the incident beam intensity. The coefficient μ is called the *total linear attenuation coefficient* and is the probability per unit path length for removal of a photon. It is the sum of three contributions

$$\mu = \tau + \sigma_c + \kappa \tag{3.2}$$

where τ, σ_c and κ are the probabilities per unit path length for photoelectric effect, Compton scattering and pair production respectively. The probability for a reaction to occur is governed by the *cross section*, σ. The total probability per unit path length for a photon to interact in a matter corresponds to the sum of individual cross sections, one for each kind of interaction. The relation between μ and σ is

$$\mu = \sigma \, \frac{\rho N_A}{A} \tag{3.3}$$

where N_A is the Avogadro's constant, ρ is the density of the matter and A the mass number.

The average distance traveled in matter for a γ-ray photon without suffering a collision is defined by their *mean free path*, λ, and is obtained from

$$\lambda = \frac{\int_0^\infty x e^{-\mu t} dt}{\int_0^\infty e^{-\mu t} dt} = \frac{1}{\mu} \tag{3.4}$$

3.1.1 Photoelectric Effect

In the photoelectric effect process, a photon is absorbed by an atomic electron which results in ejecting the electron from its electron shells. The kinetic energy of this electron, called *photoelectron*, is

$$E_{e^-} = E_\gamma - E_b \tag{3.5}$$

that is, the energy of the incident photon, $E_\gamma = hv$, minus the binding energy of the electron, E_b. This binding energy is liberated either as Auger electrons, where the atom de-excites by releasing other less tightly bound electrons, or where electron from higher shell fills the vacancy created with emission of characteristic X-ray photons. Photoelectric effect always takes place on bound electrons due to conservation of momentum.

An approximate expression of the photoelectric probability is

$$\tau \propto \frac{Z^n}{E_\gamma^{7/2}} \tag{3.6}$$

where n varies between 4 and 5 and Z is the atomic number [5].

3.1.2 Compton Scattering

An incoming γ-ray photon with energy E_γ scatters off a free electron considered to be at rest and deflects through an angle θ. The energy of the scattered photon is

$$E_{\gamma'} = \frac{E_\gamma}{1 + \frac{E_\gamma}{m_0 c^2}(1 - \cos\theta)} \tag{3.7}$$

where $m_0 c^2$ is the rest-mass energy of the electron, 0.511 MeV. The electron recoils with an amount of kinetic energy $E_{e^-} = E_\gamma - E_{\gamma'}$.

The probability of Compton scattering, σ_c, depends on the density of electrons in the medium and therefore the cross section per atom increases linearly with Z. It is generally inversely proportion to the γ-ray energy, E_γ [5].

3.1.3 Pair Production

Pair production involves the replacement of a γ-ray photon by an electron/positron pair. For this to be energetically possible the γ-ray has to have energy exceeding 1.022 MeV or twice the rest-mass energy of an electron. The kinetic energy of the electron/positron pair is given by

$$E_{e^-} + E_{e^+} = E_\gamma - 2m_0 c^2 \tag{3.8}$$

The magnitude of the cross section is approximately proportional to the square of the atomic number Z^2 [5].

The positron is not a stable particle, it quickly slows down and annhiliates with an electron in the absorbing material. The particles are converted into two oppositely directed γ-rays, each of energy 0.511 MeV.

3.2 Interaction of Electrons and Positrons

When passing through matter, electrons and positrons lose energy by interacting with atomic electrons through *Coulomb scattering*, that is elastic scattering in a Coulomb field obtained by treating the particles as point charges. Due to their low mass, the particles may suffer sudden changes in direction and speed corresponding acceleration, which leads to the particles to radiate electromagnetic energy called *bremsstrahlung*. This is dependent on the strength of the electric field felt by the electron/positron and therefore on the screening from the atomic electrons surrounding the nucleus.

The rate of energy loss per unit path length for a particle within a material is called *stopping power*, $-(dE/dx)$. The total energy loss of electrons and positrons is defined as the sum of the collisional losses, that is energy loss due to ionization and excitation, and radiative losses [5]

$$\left(\frac{dE}{dx}\right)_{\text{tot}} = \left(\frac{dE}{dx}\right)_{\text{coll}} + \left(\frac{dE}{dx}\right)_{\text{rad}} \tag{3.9}$$

where

$$-\left(\frac{dE}{dx}\right)_{\text{coll}} = \frac{2\pi Z}{\beta^2}\frac{e^4}{(4\pi\epsilon)^2 m_0 c^2}\frac{\rho N_A}{A}\left(\ln\frac{m_0\nu^2 E}{2I^2(1-\beta^2)} - (\ln 2)(2\sqrt{1-\beta^2} - 1 + \beta^2) + (1-\beta^2) + \frac{1}{8}(1-\sqrt{1-\beta^2}\,)^2\right) \tag{3.10}$$

and

$$-\left(\frac{dE}{dx}\right)_{\text{rad}} = 4\alpha Z(Z+1)E\frac{e^4}{(4\pi\epsilon)^2 m_0^2 c^4}\frac{\rho N_A}{A}\left(\ln\frac{2E}{m_0c^2} - \frac{4}{3}\right) \tag{3.11}$$

Here $\alpha \approx 1/137$ is the fine structure constant, ρ and Z are the density and the atomic number of the absorber atom, N_A and A are the Avogadro's constant and the mass number as before, and I represents the average excitation and ionization potential of the absorber. The parameter β is defined as $\beta = \nu/c$ where ν is the velocity of the primary particle, here electron or positron, and E is its kinetic energy. The electron rest mass and electronic charge are represented with m_0 and e.

A critical energy, E_c, is defined for an absorber material as the energy for which energy loss by radiation equals the collision losses [6]

$$E_c \approx \frac{800\ \text{MeV}}{Z + 1.2} \tag{3.12}$$

Above E_c radiation losses will dominate over collision losses.

Radiation Length

Radiation length, X_0, of a material is the distance the electron has traveled after which the electron energy is reduced by a factor $1/e$ due to radiation losses only. It is given by [6]

$$\frac{1}{X_0} \approx 4\alpha Z(Z+1)\frac{e^4}{(4\pi\epsilon)^2 m_0^2 c^4}\frac{\rho N_A}{A}\left(\ln\left(\frac{183}{Z^{1/3}}\right) - f(Z)\right) \tag{3.13}$$

where the symbols have the same meaning as in equations (3.10) and (3.11). The function $f(Z)$ is a small correction due to the Coulomb interaction of the emitting electron in the electric field of the nucleus.

The mean free path of a γ-ray photon for pair production is related to the radiation length, i.e.

$$\lambda_{\text{pair}} \approx \frac{9}{7} X_0 \tag{3.14}$$

Moliere Radius

When a material is struck by γ-rays or electrons, the particles radiate their energy by creating a shower of secondary photons and electrons. A measure of transversal distribution of this so-called electromagnetic shower is given by the *Moliere radius*, R_M [6]

$$R_M = X_0 \frac{21.2 \text{ MeV}}{E_c} \tag{3.15}$$

where E_c is the critical energy.

4 Light Yield Uniformity Measurements

Light yield uniformity measurements were performed on the lead tungstate crystals. A photon hits a scintillating material which is connected to a photomultiplier tube, and deposits energy. Photoelectrons are releases from the photocathode of the tube. The number of these photoelectrons per the deposit energy is defined as light yield. Nonuniformity means that the light yield from a scintillating material is dependent on the interaction point of the photon, that is where the energy is deposit in the material. This can impair the energy resolution.

4.1 Instrumentation

Scintillator detector

A scintillator detector consists of a scintillating material and a photo sensor, in this case a photomultiplier tube. When ionizing radiation passes through a scintillation material, atoms or molecules are excited to states which decay under emission of photons, a process called *luminescence*. These photons are then transmitted to the photomultiplier tube. If the decay occurs immediately after the transition to excited state, within 10^{-8} s, it is called *fluorescence*. However, if the electrons arrive to excited states which are metastable, it results in a delay in the decay, and the process is called *phosphorescence* or *afterglow*. This delay time depends on the scintillating material and can take values from a few microseconds to hours [6].

The electrons can be excited to excited states where a decay without emission of a photon is possible. This effect is called *quenching* and reduces the intensity of the emitted light. This can be compensated for, i.e. by decreasing the temperature of the scintillating material.

For inorganic scintillators the radiation excites electrons across the *energy gap*, from the *valence band* into the *conducting band*, creating *electron-hole pairs*. The electron then looses energy by emitting a photon and returns to the valence band. To enhance the probability for photon emission and for the material to be transparent to its own radiation, a small amount of impurities, called *activators*, are added to the crystal. These impurity atoms provide states within the energy gap resulting in photon emission to take place between the activator states.

The photomultiplier tube

A photomultiplier tube, (PM tube), consists of a photosensitive layer, called the *photocathode* and a series of electrodes called *dynodes*. The electrodes are connected to a resistor chain over which a voltage is applied to create an electric field between the dynodes. The scintillation photons strikes the *photocathode* and electrons are emitted via the photoelectric effect. These electrons, called *photoelectrons*, are directed and accelerated by the internal electric field to hit the first dynode. Secondary electrons are released and accelerated towards the next dynode where more electrons are released. Thus a multiplication process takes place. Finally all the electrons are collected at an *anode*. The current at the output is proportional to the number of incident photons.

Electrons in the conduction band have thermal kinetic energy which can exceed the potential barrier of the cathode. This can lead to escape of an electron, creating an induced signal. This is called *thermionic noise*. This noise increases with increasing temperature of the cathode.

Quantum efficiency of the photomultiplier tube is defined as the number of photoelectrons emitted per incident photon. It highly depends on the wavelength of the incident light. The spectral response is, in general, only efficient over a certain band of wavelengths. Therefore, one consideration when choosing a PM tube is to have a high quantum efficiency over the wavelength of the incident light.

The gain at each dynode is given by the *multiplication factor*, δ, which is the average number of secondary electrons emitted per primary electrons. The multiplication factor is a function of the energy of the primary electron and therefore a function of the applied voltage. For n number of dynodes the overall gain G in the photomultiplier tube is

$$G = \delta^n = (KV)^n \tag{4.1}$$

where V is the applied voltage and K is a proportionality constant.

4.2 Energy Resolution

When measuring the energy of incident radiation with a scintillator detector, the energy distribution can fluctuate around its mean value. These fluctuations contribute to the energy resolution of the detector. Ideally, measured quantity should appear as a delta-function peak, however the shape of the peak is usually Gaussian with a finite width [6]. This width is due to the fluctuations.

The relative energy resolution of the scintillator detector is defined as the relative standard deviation

$$R_E = \frac{\sigma_E}{\bar{E}} \tag{4.2}$$

with $\bar{E}$ as the mean value of the measured energy distribution and σ_E the standard deviation. There are a number of contributions to the energy resolution. The variation in light collected from scintillation events due to nonuniformity of the crystals can contribute to the energy resolution, see above. The measured energy distribution can fluctuate because of energy leakage from the detector. The Poisson statistics of the light collection process in the scintillating material influence the resolution (see section 4.5). Effects from the electronics used in the measurements, such as noise, varying high voltage, etc, have to be considered. The total energy resolution is therefore a sum of all these contributions, and given by

$$\sigma_E^2 = \sigma_\beta^2 + \sigma_{\text{leak}}^2 + \sigma_{\text{Poiss}}^2 + \sigma_{\text{elect}}^2 + \dots \tag{4.3}$$

4.3 The $PbWO_4$ Crystals

Eleven lead tungstate, PWO, scintillation crystals of different shapes for the barrel were studied, the shapes are presented in table 4.1. The crystals are all 20 cm long, of type LEFT and have two corners where all angles are 90°.

The crystals were produced at the Bogoroditsk Technical Chemical Plant in Russia. They are very compact, as can be seen from the high density, ρ, and the short radiation length, X_0, and with good radiation hardness. The PWO material has extremely short decay kinetics, in which the short decay constant, τ_{decay}, is dominant (97%). Therefore pile-up effects can be kept low in the scintillator, even at high count rates [7]. However, the light yield from PWO is very low, or only 1.2% of the light yield from NaI scintillating material [7]. Table 4.2 shows some of PWO properties. The quantity (dE/dx) is the rate of energy loss per unit path lenght for minimum ionizing electrons in PWO.

Type	Volume [cm^3]	θ_B [°]	θ_A [°]	θ_C [°]
1	126.86	2.1	2.2	2.2
2	126.56	2.1	2.1	2.2
3	125.79	2.1	2.1	2.1
4	120.85	1.7	1.9	2.0
5	119.69	1.7	1.8	1.8
6	118.35	1.7	1.6	1.6
7	112.90	1.2	1.4	1.5
8	111.75	1.2	1.3	1.3
9	110.52	1.2	1.1	1.2
10	107.01	0.9	1.0	1.0
11	106.25	0.9	0.9	0.9

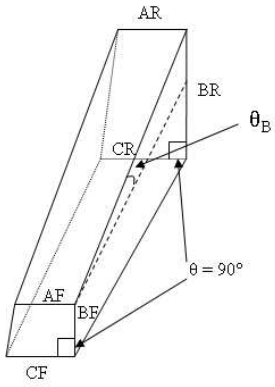

Table 4.1: The geometric shape of the 11 PWO crystals. All the crystals are 20 cm long, of type LEFT and have two corners where all angles are 90°. The definition of angle θ_B is shown. F stands for the front end of the crystal and R for the rear end where the photo sensor is attached.

Figure 4.1: A photograph of PWO crystals. The crystals used in this measurement were more tapered in shape. From [7].

Parameter	$PbWO_4$
ρ	8.28 g/cm^3
X_0	0.89 cm
R_M	2.0 cm
τ_{decay}	6 ns
λ_{max}	420 nm
dE/dx	13 MeV/cm

Table 4.2: Some properties of the PWO material. From [7].

4.4 The Set-up

In order to deposit a certain amount of energy at a given position in the PWO crystal a ^{22}Na source was used. It decays via β^+:

$$^{22}_{11}\mathrm{Na} \quad \rightarrow \quad ^{22}_{10}\mathrm{Ne}^* + e^+ + \nu_e$$

emitting a positron e^+ and a neutrino ν_e. The positron annhiliates with an electron in the surrounding material of the source and two 511 keV γ-rays are emitted in opposite directions. The excited state of ^{22}Ne quickly decays with γ-emission of energy 1.275 MeV.

To determine the position of where a γ-ray enters the PWO crystal, coincident measurements were done. The source was located between the PWO crystal and a small BaF detector, see figure 4.2. By detecting one of the annhiliation γ-rays in the BaF detector the impact point on the PWO crystal of the other γ-ray is know with some precision. The BaF detector and the source was slided along the PWO crystal and signals were collected for a live time of $\tau = 900$ s.

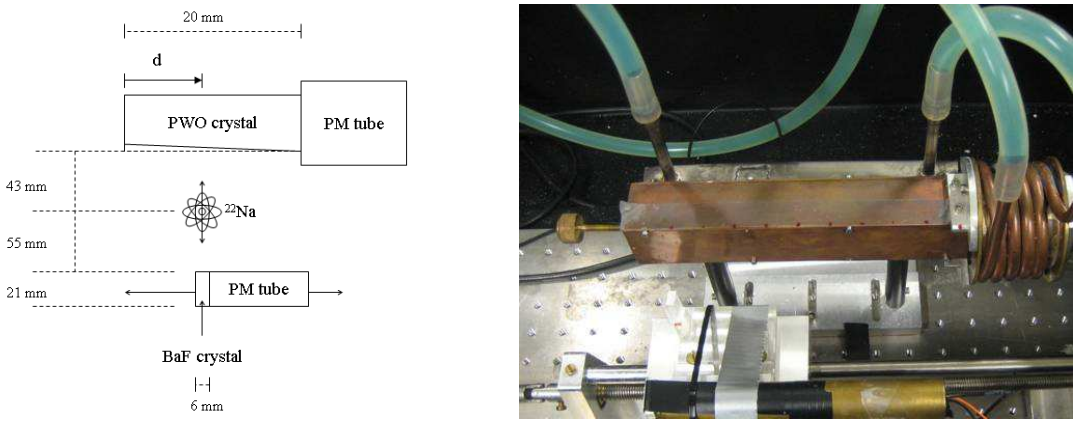

Figure 4.2: The set-up for the uniformity measurements. (a) ^{22}Na source is located between the two scintillators. By detecting the two annihilation γ-rays, the position of the incoming γ-ray striking the PWO crystal is known. The parameter d describes the distance from the front face of the PWO crystal towards the PM tube. (b) A photograph of the set-up.

The PM tube was of type Hamamatsu R2083. It fully coved the rear-end of the crystal. Figure 4.3 shows the wavelength dependence for the response of the PM tube, the maximum quantum efficiency is reached for wavelength around 400 nm. This is close to the wavelength of maximum emission, λ_{max}, of the PWO material, see table 4.2. The crystals were wrapped in reflective material, *VM2000*, to maximize the light yield and were in contact with the entrance window of the PM tube via optical grease, *Visilox*. The set-up was inside a black box to shield the PM tube from ambient room light and cooled down to a temperature $T = 5$°C.

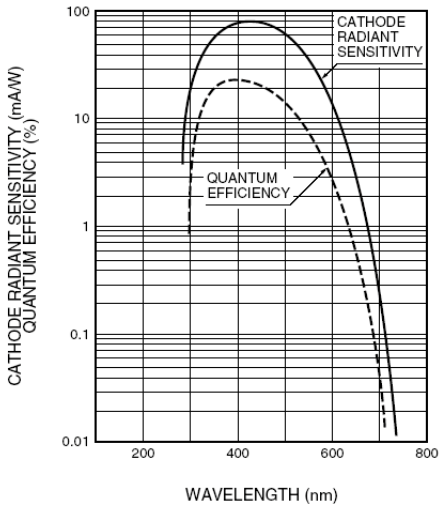

Figure 4.3: The quantum efficiency for a PM tube of type Hamamatsu R2083. From [8].

The electronics were located outside the box, see figure 4.4. A gate signal was sent to a Multi-Channel Analyzer, Tukan 8k, only if there was a signal in the BaF detector corresponding to 511 keV. The signal from the PWO crystal was amplified before being passed to Tukan 8k. The amplifier had 1 μs shaping time.

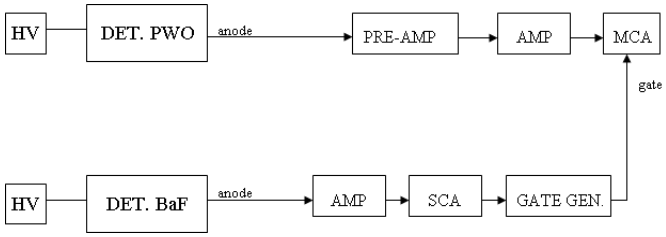

Figure 4.4: The electronic set-up.

4.5 Calibration of the Photoelectron Spectrum

The production of secondary electrons in the photomultiplier tube is a statistical process, meaning that the number of secondary electrons will be different between events, resulting in fluctuation in gain. By examine the shape of a single photoelectron pulse height spectrum, this fluctuation can be measured.

It is possible to assume that the number of secondary electrons follow a Poisson distribution [5]. For N_{pe} numbers of photoelectrons incident on the first dynode, the mean value and the standard deviation of number of secondaries emitted are therefore expressed as

$$\bar{N}_{pe} = N_{pe}\delta \quad , \quad \sigma_{N_{pe}} = \sqrt{N_{pe}\delta} \tag{4.4}$$

where δ is the multiplication factor. The relative variance, that is the spread in the number of secondary electrons, is then

$$\left(\frac{\sigma_{N_{pe}}}{\bar{N}_{pe}}\right)^2 = \frac{1}{(N_{pe}\delta)} \tag{4.5}$$

Therefore, having n number of dynodes, each with the same multiplication factor, the relative variance of the final signal becomes

$$\frac{1}{(N_{pe}\delta)} + \frac{1}{(N_{pe}\delta)^2} + \frac{1}{(N_{pe}\delta)^3} + \cdots + \frac{1}{(N_{pe}\delta)^n} \approx \frac{1}{N_{pe}\delta - 1} \tag{4.6}$$

where the limit $N \to \infty$ has been used as an approximation [5].

Tukan 8k, the Multi-channel Analyzer, was calibrated by using the linear relation

$$k = a + bN_{pe} \tag{4.7}$$

Here k is the pulse-height (in channel number), N_{pe} is the number of photoelectrons, a is the zero offset and b is the difference in pulse-height corresponding to one photoelectron. Pulse height spectrum was measured under poor light collection conditions such that the probability of more than a few photoelectrons contributing to each pulse is small. Therefore is was possible to distinguish the peaks matching a few photoelectrons. In the spectrum, peaks corresponding to $N_{pe} = 1$, 2 and 3 were noticed, see figure 4.5.

The interval between channel 75 and 330 was fitted with five Gaussian distributed peaks, corresponding to $N_{pe} = 1$, 2, 3, 4 and 5. It was assumed that more photoelectrons did not contribute in the interval chosen. The centroids of the Gaussians, $k_{N_{pe}}$, corresponded to the number of incident photoelectrons, according to equation (4.7). The standard deviation for each Gaussian was evaluated from equation (4.6) as

$$\sigma_k = b\,\frac{N_{pe}}{\sqrt{N_{pe}\delta - 1}} \tag{4.8}$$

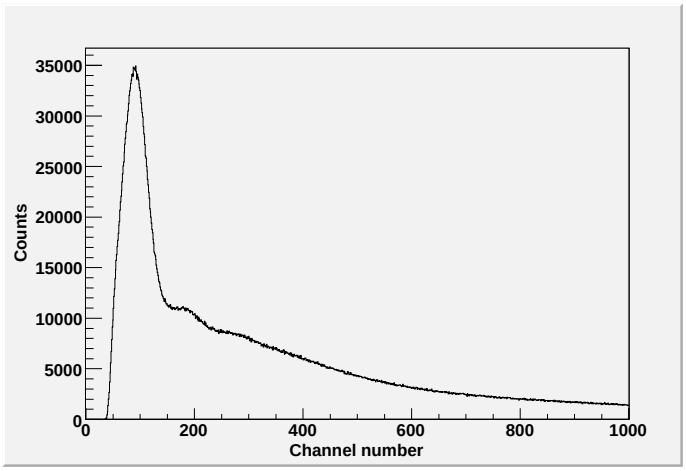

Figure 4.5: Measured pulse height spectrum under poor light collection condition. The peak corresponding to a single photoelectron can be seen clearly, the peaks for $N_{pe} = 2, 3$ photoelectrons are more vague.

The fitted coefficients a and b were given start values using rough estimation from figure 4.5 and the multiplication factor was put to $\delta = 10$. The amplitude of the five Gaussian were also given initial values.

$$\begin{array}{rcrcl} a & = & 10.30 & \pm & 0.04 \\ b & = & 78.25 & \pm & 0.02 \\ \delta & = & 9.97 & \pm & 0.03 \end{array}$$

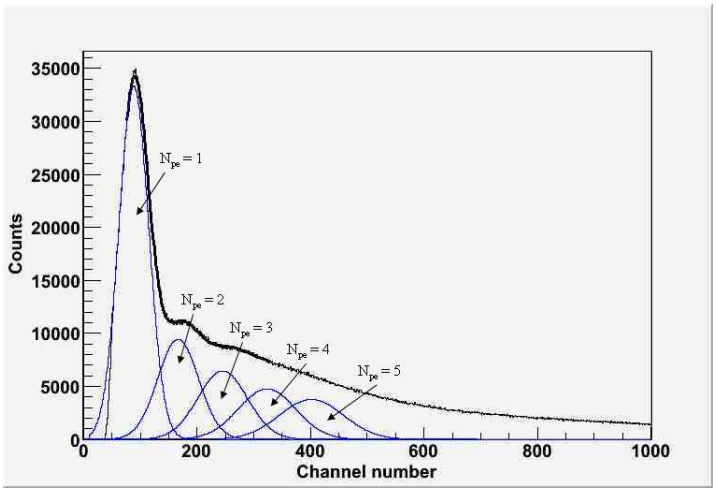

Figure 4.6: Measured pulse height spectrum for calibration (fulldrawn, thin). A χ^2 fit between channel numbers 75 and 330 yielded the full drawn curve (full drawn, thick). The separate five Gaussian contributions are shown (full drawn, blue). The χ^2/n.d.f. = 730.3/248.

4.6 Light Yield Measurements

Figure 4.7 shows a typical pulse height spectrum. All spectra were corrected for random coincidences, that is measurements were performed as before but the annhiliation γ-rays were not coincidence in time. These spectra were then subtracted from the spectra of the coincidence measurements.

The peak corresponding to 511 keV shifted between different impact points of the γ-rays, the centroid of the peak increased as the distance from the PM tube got larger. This is a sign of a nonuniform light yield. To quantify this the peak for 511 keV was fitted with a Gaussian distribution and a background described by a polynomial of degree 1 with the program Tukan 8k. By using the relation in equation (4.7) and the values for a and b, the number of incident photoelectrons corresponding to the centroid of the peak, N_{pe}, was calculated. This number was normalized to obtain the number of photoelectrons per unit energy, β, by dividing by the incoming energy $E_\gamma = 511$ keV. Thus $\beta = N_{pe}/E_\gamma$. The energy was taken to be equal 511 keV but is in reality little less due to Compton scattering of the γ-ray photon in the crystal and X-ray escape. The value of the energy only scales the result for all β in the same way. The uncertainties in β were calculated with the error propagation formula and errors were assumed in the peak position as well as in the coefficients a and b.

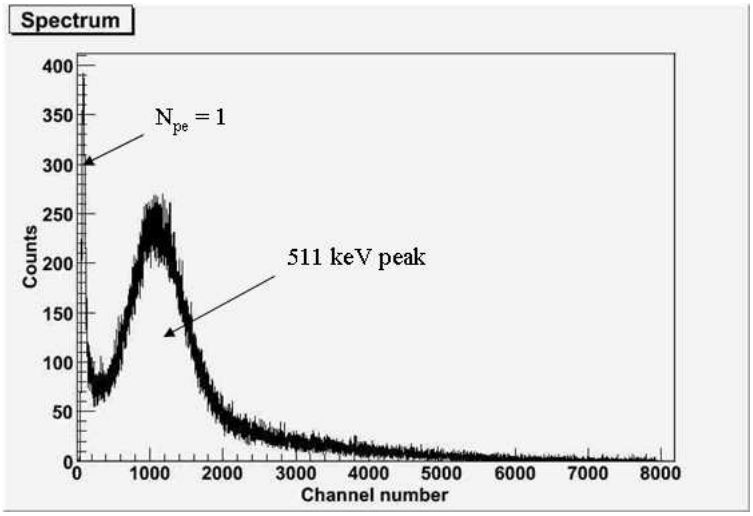

Figure 4.7: Typical pulse height spectrum for 511 keV photon.

4.7 Temperature Measurements

Due to strong temperature quenching in PWO, the measured light yield, β_m, is very temperature dependent [1]. In order to correct the measured values of β_m to correspond to a constant temperature, the temperature along the crystal was measured. As can be seen in figure 4.8 the temperature varies along the crystal, the largest difference being around 0.5 °C, between the middle of the crystal and the front end.

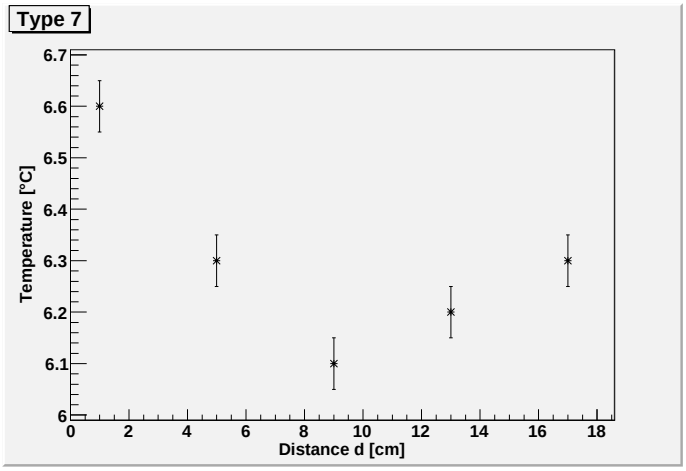

Figure 4.8: Temperature varies along the crystal, the distance $d = 0$ cm is furthest away from the photomultiplier tube. Measurements were performed on crystal of type 7.

Figure 4.9 shows the pulse height spectrum for two different temperature values, $T = 5$°C and $T = 7$°C. The figure reveals that the light yield increases as the temperature decreases. The temperature difference of 2°C gave 4.4% shift of 511 keV peak. Figure 4.10 shows the light yield as a function of distance for crystal of type 1 before and after temperature correction. The light yield was compensated for the temperature effect by inter and extrapolating the temperature along the crystals. Even though the crystals were cooled down nominally to $T = 5$°C, the reference temperature measured around the crystal was $T = 6.3$°C.

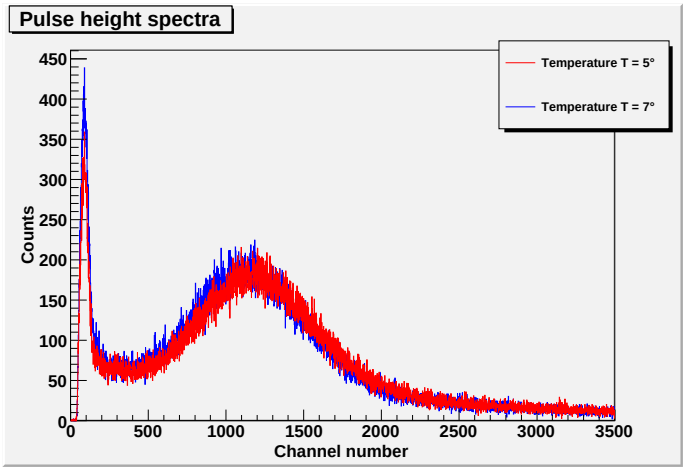

Figure 4.9: Pulse height spectra recorder at two different temperatures. The shift of the centroid is approximately 4.4%.

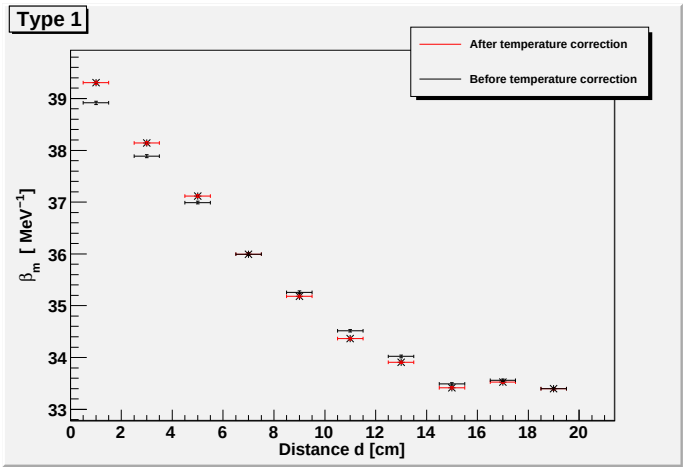

Figure 4.10: The light yield, β_m, as a function of distance before and after temperature correction.

4.8 Fitting Interval

When fitting the peak with a Gaussian function, the choice of interval around the peak can affect the result and leed to systematic errors. In the analysis a first estimate of the peak position was done by a fit in a predetermined interval, the same in all spectra for each crystal. This interval was large enough to fully cover the peaks. Then a new corrected interval of the same width was chosen, centered around the estimated peak position, and a new fit was done to find the peak position. Figure 4.11 shows the measured light yield, β_m, as a function of distance, d, before and after the correction. The largest correction of β_m is around 0.6%.

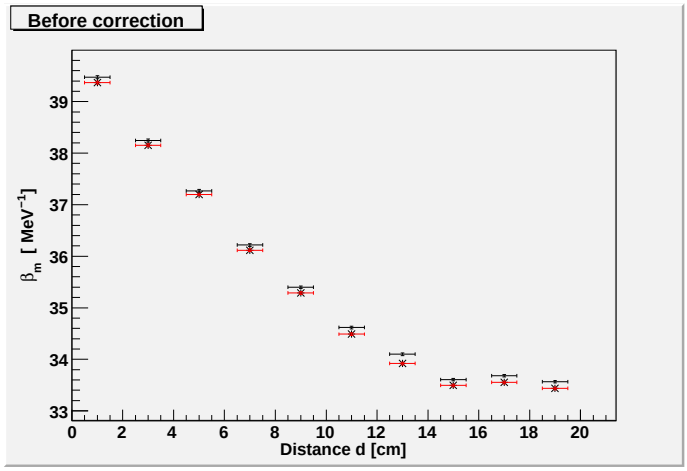

(a)

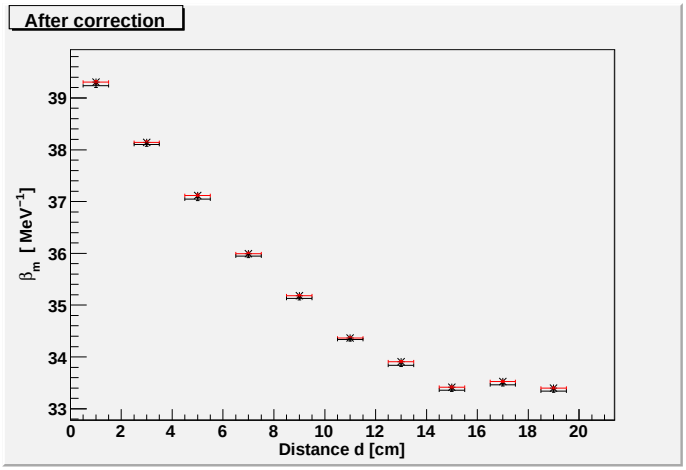

(b)

Figure 4.11: The light yield, β_m, for the crystal of type 1 as a function of distance, d. The Gaussian distribution fitted to the peak corresponding to 511 keV was affected by the interval chosen. This was compensated for by finding the final peak position in an interval centered around an estimated peak position. (a) The light yield before the correction, two different predetermined intervals were chosen and the peak positions calculated. The largest shift is around 0.6%. (b) The light yield after the correction of the two predetermined intervals. Shift in β_m is negligible.

4.9 The Measured Light Yield

Figures 4.12 and 4.13 show the measured light yield, β_m, as a function of distance, d. As can be seen the light yield is very dependent on the shape of the crystals, crystals with a larger tapering give larger variation in the light yield output. The mean value of the light yield, $\bar{\beta}_m$, was calculated as well as the nonuniformity for each of the eleven crystals, α_{nu}. These values are presented in table 4.3.

Table 4.3: Mean value of light yield $\bar{\beta}_m$ and nonuniformity $\sigma_{\beta_m,\text{rel}}$. Comparison to a forward end cap crystal is done [9].

Type	Volume [cm^3]	θ_B [°]	θ_A [°]	θ_C [°]	$\bar{\beta}_m$ [MeV^{-1}]	α_{nu} [%]
1	126.86	2.1	2.2	2.2	35.4 ± 0.9	6.01 ± 0.06
2	126.56	2.1	2.1	2.2	34.6 ± 0.9	8.22 ± 0.08
3	125.79	2.1	2.1	2.1	38.7 ± 0.8	5.89 ± 0.07
4	120.85	1.7	1.9	2.0	26.8 ± 0.6	6.52 ± 0.07
5	119.69	1.7	1.8	1.8	31.9 ± 0.8	7.21 ± 0.07
6	118.35	1.7	1.6	1.6	31.4 ± 0.6	5.93 ± 0.08
7	112.90	1.2	1.4	1.5	27.6 ± 0.5	5.34 ± 0.07
8	111.75	1.2	1.3	1.3	31.9 ± 0.5	4.28 ± 0.08
9	110.52	1.2	1.1	1.2	31.5 ± 0.3	2.40 ± 0.10
10	107.01	0.9	1.0	1.0	30.6 ± 0.3	2.99 ± 0.08
11	106.25	0.9	0.9	0.9	25.4 ± 0.3	2.70 ± 0.10
Forward end cap crystal			0.5		21.5	0.9

To estimate the nonuniformity of the crystals, the spread of the light yield is calculated as the relative standard deviation

$$\alpha_{\text{nu}} = \frac{\sigma_{\beta_m}}{\bar{\beta}_m} \tag{4.9}$$

where the the mean value is

$$\bar{\beta}_m = \frac{1}{n}\sum_{i=1}^{n}\beta_m(i) \tag{4.10}$$

and the standard deviation

$$\sigma_{\beta_m} = \left(\frac{1}{n-1}\sum_{i=1}^{n}(\beta_m(i) - \bar{\beta}_m)^2\right)^{\frac{1}{2}} \tag{4.11}$$

Here n is the number of measuring points and $\beta_m(i)$ the measured number of photoelectrons per unit energy at the i:th point. The nonuniformity α_{nu} should be 0 for a totally uniform light yield.

The uncertainty in the mean value $\bar{\beta}_m$ is found from the spread

$$\Delta\bar{\beta}_m = \frac{\sigma_{\beta_m}}{\sqrt{n}} \tag{4.12}$$

The uncertainty in the nonunifromity value was calculated with the error propagation formula.

4.10 Optical Grease and Wrapping Effects

To see how the optical grease and wrapping may influence the measured light yield, the crystal of Type 4 was wrapped again with the same material, VM2000, and measured. The contact to the PM tube was broken, and the grease material, Visilox, replaced. The results before and after can be seen in table 4.4. The mean value of the light yield and the nonuniformity measure change by 20%, giving an indication of possible systematic uncertainties in these measurements.

Table 4.4: Mean value of light yield $\bar{\beta}_m$ and nonuniformity α_{nu} for crystal of Type 4, before and after wrapping the crystal.

	$\bar{\beta}_m$ [MeV^{-1}]	α_{nu} [%]
Before:	26.8 ± 0.6	6.52 ± 0.07
After:	32.2 ± 0.7	5.42 ± 0.07

4.11 Conclusion

The measured light yield of the crystals is not uniform but very dependent on the position of the impact point of the incoming γ ray photon. Larger values of light yield were measured as the distance from the PM tube increased, see figure 4.12 and 4.13. The light yield is also different for different type of crystal. The mean value differs by approximately 30% and the nonuniformity by almost 70%. Crystals that are more tapered in shape give larger nonuniformity values, as can be seen in table 4.3.

Temperature variations contribute to the measured light yield, a change of -1°C increased the light yield of 2.2%. Another factor that needs to be considered is the optical grease connecting the crystals and the PM tube as well as the wrapping. The nonuniformity and the mean value altered by 20% due to these effects for the crystal.

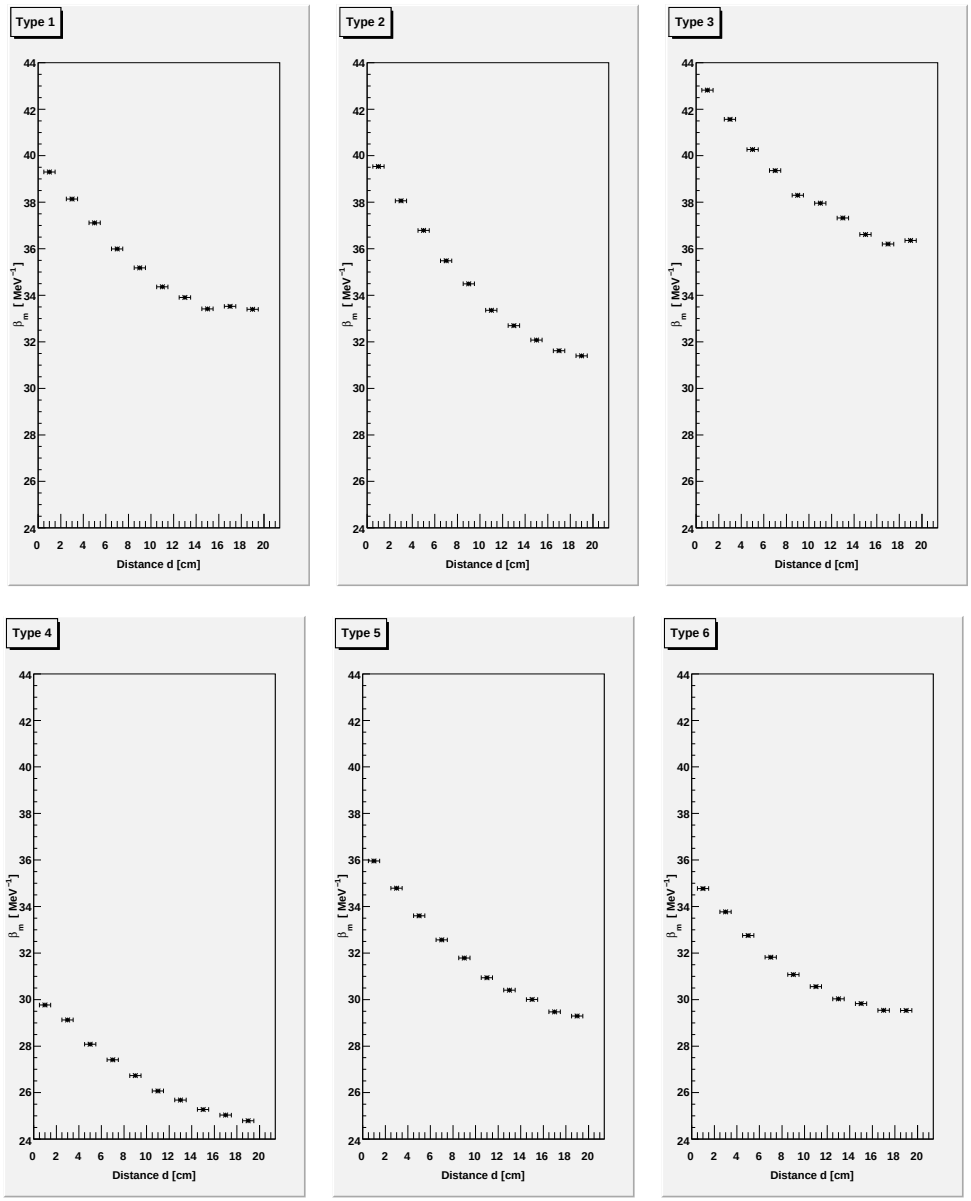

Figure 4.12: Measured light yield $\beta_m = N_{pe}/E_\gamma$ as a function of distance d. The distance $d = 20$ cm is closest to the photomultiplier tube. Crystals of type 1 - 6.

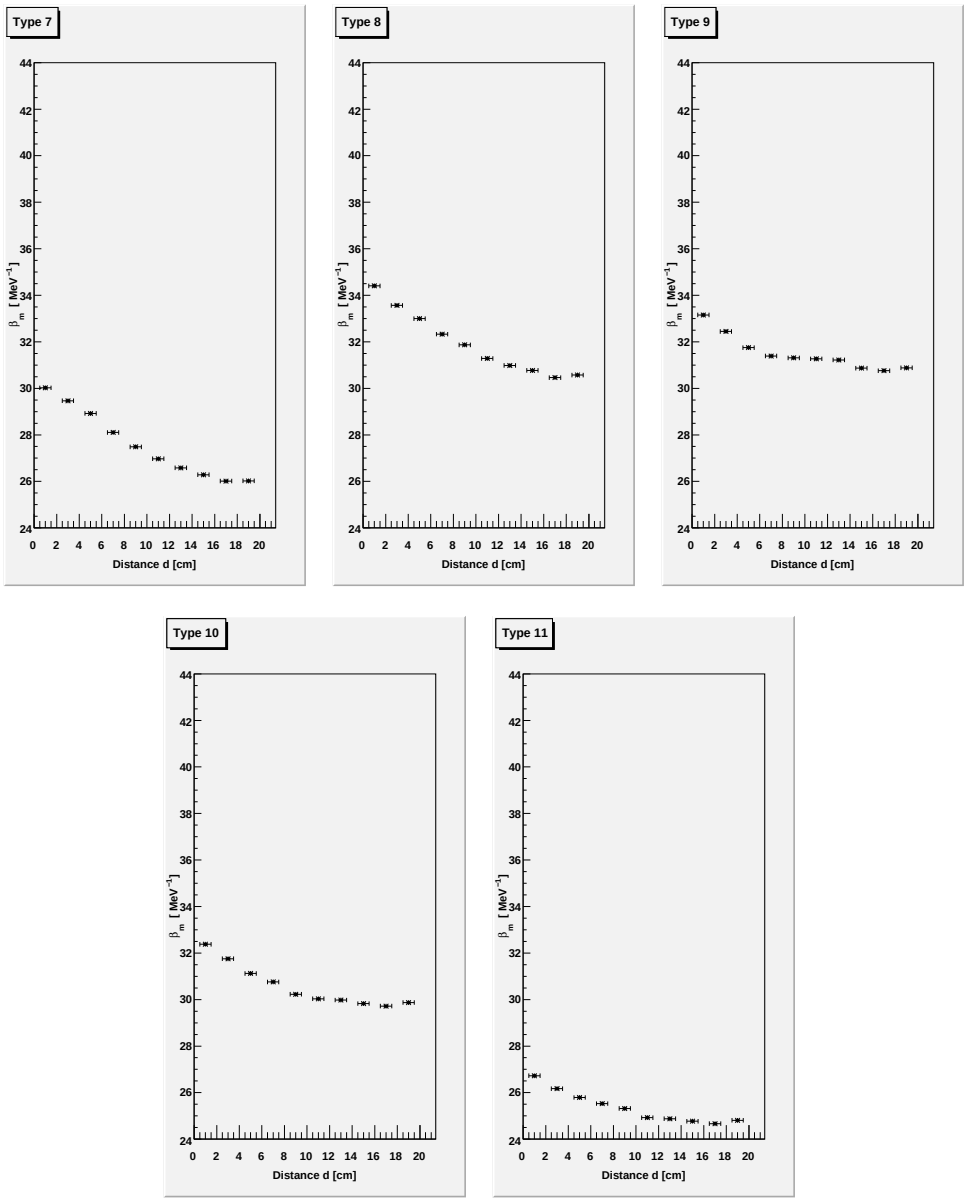

Figure 4.13: Measured light yield $\beta_m = N_{pe}/E_\gamma$ as a function of distance d. The distance $d = 20$ cm is closest to the photomultiplier tube. Crystals of type 7 - 11.

5 Geant4 Simulation

Simulation of γ-rays interaction with PWO was done with the toolkit Geant4, version 4.9.2, to obtain the depth distribution of the energy deposited in the crystal. The motivation was to find out how the nonuniformity of the light yield is affecting the energy resolution (α_{nu} in section 4.9). Geant4 is based on Monte Carlo methods, a technique that uses random numbers and probability statistics to solve problems. *Novice Example N03* was used as a skeleton [10].

5.1 Code Description

The files used in this simulation are:

- In `DetectorConstruction` the detector's geometry is defined as well as the material. The detector is located in a *World*. `DetectorMessenger` allows for build-in changes made on the detector.
- `Physics List` constructs particles, physics processes and associates them to particles. There the *cut in range* is defined for the particles and Geant4 converts it into energy threshold for each material. This means that particles with energy under this threshold are stopped and their remaining energy is dumped at that point.
- In `PrimaryGeneratorAction` the primary type of the bombarded particle and its energy is defined, it can be changed via `PrimaryGeneratorActionMessenger`.
- In `EventAction` physics components are calculated for each *event* and stored while `RunAction` stores these components for each *run*. One run is a series of events which share the same detector conditions and physics processes.
- `Stepping Verbose` creates an output which contains information of secondary events. Each particle is followed through and one physics process listed to a particle introduces a *step*. By heightening the verbose level, more detailed output is created. `Stepping Action` stores values wanted for each step.
- `VisManager` allows visualization of the detector, materials and the trajectories of the particles.
- *RanecuEngine* from the module CLHEP is used to create the random numbers needed.

5.2 Simulation

In order to obtain the depth distribution of the energy deposition, a stack of 20 PWO layers, each having thickness 1 cm, was set up. The lateral dimensions were set to 2 m to avoid lateral leakage, see figure 5.1. The energy deposited in every layer was stored. The stack was placed in vacuum. The particles used for this simulation were γ-ray photons, electrons and positrons. The physics processes *Transportation* and *Standard electromagnetic process* were also used.

The "Standard electromagnetic process" created gamma and electron/positron processes. The gamma processes handled *photoelectric effect*, *Compton scattering* and *pair production* while electron/positron processes handled *scattering*, *bremsstrahlung*, *ionization* and *positron annihilation*. To estimate which process a particle in flight should undergo, the cross sections for each processes are calculated and Monte Carlo methods are used.

A high energy photon hit the 20 cm thick wall of PWO and produced an event. This particle was followed through as well as every secondary particle it created. The cut in range was 1 mm for each particle giving energy thresholds shown in table 5.1

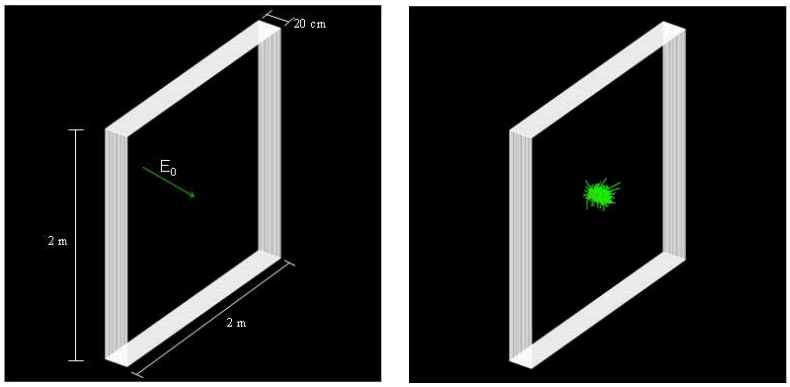

(a) (b)

Figure 5.1: Geant4 visualization. The stack consists of 20 PWO layers, each having thickness 1 cm and lateral dimensions 2 m to mimic the PANDA calorimeter with 20 cm long crystals. (a) A γ-ray particle of energy E_0. (b) A γ-ray particle having initial energy $E_0 = 10$ GeV hits the stack revealing no lateral leakage.

Table 5.1: The energy thresholds calculated with Geant4 for cut in range as 1 cm.

	gamma	electron	positron
Vacuum:	990 eV	990 eV	990 eV
PWO:	84.78 keV	1.13 MeV	1.06 MeV

Figure 5.2 shows one γ-ray of initial energy $E_0 = 20$ MeV hitting the crystal array and its interactions while figure 5.3 shows the output.

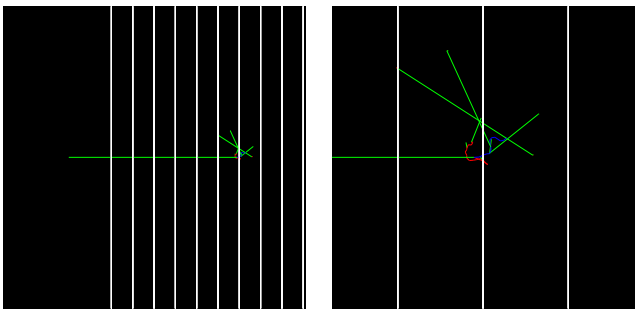

(a) (b)

Figure 5.2: Geant4 visualization, longitudinal view of the stack. (a) The PWO layers are irradiated by one 20 MeV gamma ray. Green lines are gamma ray trajectories, red lines are the trajectories of electrons and blue lines are positrons. (b) Closer look.

```
### Run 0 start.

*****************************************************************************************************
* G4Track Information:   Particle = gamma,   Track ID = 1,   Parent ID = 0
*****************************************************************************************************

Step#      X         Y         Z        KineE    dEStep   StepLeng  TrakLeng    Volume     Process
    0    -12 cm      0 fm      0 fm     20 MeV     0 eV      0 fm      0 fm        World    initStep
    1    -10 cm      0 fm      0 fm     20 MeV     0 eV      2 cm      2 cm        World  Transportation
    2     -9 cm      0 fm      0 fm     20 MeV     0 eV      1 cm      3 cm          PWO  Transportation
    3     -8 cm      0 fm      0 fm     20 MeV     0 eV      1 cm      4 cm          PWO  Transportation
    4     -7 cm      0 fm      0 fm     20 MeV     0 eV      1 cm      5 cm          PWO  Transportation
    5     -6 cm      0 fm      0 fm     20 MeV     0 eV      1 cm      6 cm          PWO  Transportation
    6     -5 cm      0 fm      0 fm     20 MeV     0 eV      1 cm      7 cm          PWO  Transportation
    7  -4.11 cm      0 fm      0 fm      0 eV      0 eV   8.94 mm   7.89 cm          PWO        conv
    :----- List of 2ndaries - #SpawnInStep=  2(Rest= 0,Along= 0,Post= 2), #SpawnTotal=  2 ---------------
    :  -4.11 cm      0 fm      0 fm   10.7 MeV        e-
    :  -4.11 cm      0 fm      0 fm   8.24 MeV        e+
    :---------------------------------------------------------------- End0f2ndaries Info ---------------

*****************************************************************************************************
* G4Track Information:   Particle = e+,   Track ID = 3,   Parent ID = 1
*****************************************************************************************************

Step#      X         Y         Z        KineE    dEStep   StepLeng  TrakLeng    Volume     Process
    0  -4.11 cm      0 fm      0 fm   8.24 MeV     0 eV      0 fm      0 fm          PWO    initStep
    1  -4.05 cm   31.6 um    165 um   7.66 MeV   578 keV   648 um    648 um          PWO         msc
    2     -4 cm    261 um    162 um   7.24 MeV   422 keV   550 um    1.2 mm          PWO  Transportation
    3  -3.96 cm    414 um    134 um    6.9 MeV   341 keV   489 um   1.69 mm          PWO         msc
    4  -3.93 cm    412 um  -22.2 um   6.09 MeV   457 keV   283 um   1.97 mm          PWO       eBrem
    :----- List of 2ndaries - #SpawnInStep=  1(Rest= 0,Along= 0,Post= 1), #SpawnTotal=  1 ---------------
    :  -3.93 cm    412 um  -22.2 um    359 keV     gamma
    :---------------------------------------------------------------- End0f2ndaries Info ---------------
    5  -3.92 cm    482 um   -115 um   5.73 MeV   155 keV   154 um   2.12 mm          PWO       eBrem
    :----- List of 2ndaries - #SpawnInStep=  1(Rest= 0,Along= 0,Post= 1), #SpawnTotal=  2 ---------------
    :  -3.92 cm    482 um   -115 um    203 keV     gamma
    :---------------------------------------------------------------- End0f2ndaries Info ---------------
    6  -3.91 cm    883 um   -283 um   5.28 MeV   447 keV   489 um   2.61 mm          PWO         msc
    7  -3.91 cm   1.22 mm   -452 um   4.45 MeV   331 keV   396 um   3.01 mm          PWO       eBrem
    :----- List of 2ndaries - #SpawnInStep=  1(Rest= 0,Along= 0,Post= 1), #SpawnTotal=  3 ---------------
    :  -3.91 cm   1.22 mm   -452 um    494 keV     gamma
    :---------------------------------------------------------------- End0f2ndaries Info ---------------
    8  -3.92 cm   1.64 mm   -308 um    4.1 MeV   351 keV   489 um    3.5 mm          PWO         msc
    9  -3.92 cm   2.05 mm   -115 um   3.49 MeV   609 keV   489 um   3.99 mm          PWO         msc
   10   -3.9 cm    2.3 mm    184 um   3.04 MeV   457 keV   489 um   4.48 mm          PWO         msc
   11  -3.86 cm   2.35 mm    355 um   2.64 MeV   394 keV   489 um   4.97 mm          PWO         msc
   12  -3.83 cm   2.12 mm    373 um   2.21 MeV   431 keV   489 um   5.46 mm          PWO         msc
   13   -3.8 cm   1.93 mm    209 um   1.81 MeV   404 keV   489 um   5.95 mm          PWO         msc
   14  -3.76 cm   1.98 mm    137 um   1.47 MeV   340 keV   489 um   6.44 mm          PWO         msc
   15  -3.73 cm   2.25 mm    286 um    111 keV  1.36 MeV  1.33 mm   7.77 mm          PWO       eIoni
   16  -3.73 cm   2.25 mm    283 um      0 eV    111 keV  36.3 um    7.8 mm          PWO       eIoni
   17  -3.73 cm   2.25 mm    283 um      0 eV      0 eV      0 fm    7.8 mm          PWO     annihil
    :----- List of 2ndaries - #SpawnInStep=  2(Rest= 2,Along= 0,Post= 0), #SpawnTotal=  5 ---------------
    :  -3.73 cm   2.25 mm    283 um    511 keV     gamma
    :  -3.73 cm   2.25 mm    283 um    511 keV     gamma
    :---------------------------------------------------------------- End0f2ndaries Info ---------------

*****************************************************************************************************
* G4Track Information:   Particle = gamma,   Track ID = 8,   Parent ID = 3
*****************************************************************************************************

Step#      X         Y         Z        KineE    dEStep   StepLeng  TrakLeng    Volume     Process
    0  -3.73 cm   2.25 mm    283 um    511 keV     0 eV      0 fm      0 fm          PWO    initStep
    1  -3.42 cm    252 um  -1.76 mm      0 eV   69.5 keV  4.22 mm   4.22 mm          PWO        phot
    :----- List of 2ndaries - #SpawnInStep=  1(Rest= 0,Along= 0,Post= 1), #SpawnTotal=  1 ---------------
    :  -3.42 cm    252 um  -1.76 mm    441 keV        e-
    :---------------------------------------------------------------- End0f2ndaries Info ---------------
```

Figure 5.3: Beginning of an output from Geant4. Gamma particle hits the detector and each step is followed through. After six steps of *transportation* the physics process *pair production* produces two secondary particles, positron and electron. The positron *scatters* and the process *Bremsstrahlung* causes the positron to radiate gamma particle three times. Finally the positron *annhiliates* with an electron creating two 511 keV gamma particles. One of these gamma rays dislodges an electron due to *photoelectric effect* creating an electron.

5.3 Energy Depth Distribution

The energy depth distribution, dE/dx, in a 20 cm thick stack of PWO was obtained by storing the energy deposited in each layer. The stack was hit by sufficiently many ($N_\gamma = 10000$) γ rays (events) having the same initial energy, E_{in}, to be able to neglect the statistical error in the simulation. This was done for gamma rays with 11 different initial energies, E_{in}, (runs). These energies were

$$E_{in} = 10,\ 20,\ 40,\ 80,\ 160,\ 320,\ 640,\ 1280,\ 2560,\ 5120,\ 10240 \text{ MeV}.$$

The γ-ray photons interact with the PWO material and a shower of photons, electrons and positrons is created which deposit energy in the crystal material. In figure 5.4 the distribution of the total energy deposition in the stack is shown for some γ-ray energies. At all energies there is a tail towards lower energies showing that energy leaks out from the stack. At 10 MeV the escape peak for the 511 keV annhiliation photon can be seen, for other energies the bin is too wide.

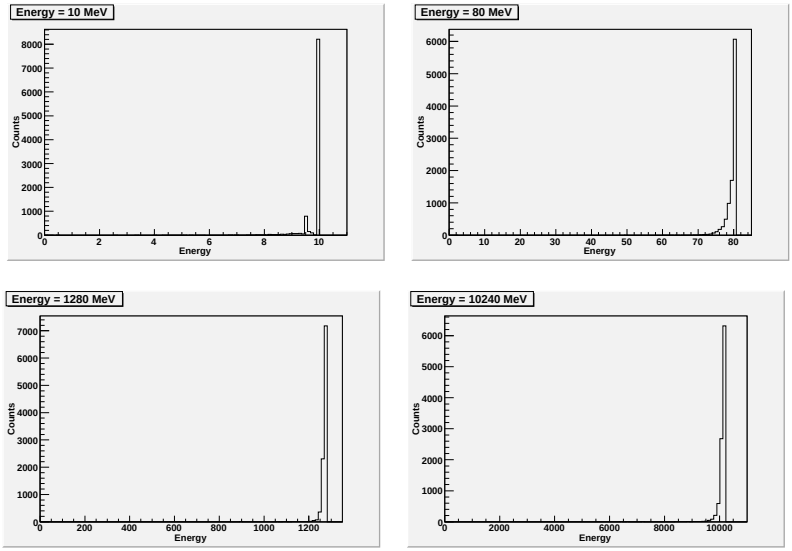

Figure 5.4: Histograms for energy distribution for $E_{in} = 10,\ 80,\ 1280$ and 10240 MeV. There is a tail toward lower energies for all energies indicating a leakage from the stack.

This is quantified in figure 5.5 where the average deposited energy (relative scale) inside the whole PWO stack as a function of incoming energy is shown. A maximum energy, relative to the incoming energy, is deposited for photons with energies around $E_{in} \approx 500$ MeV. The behavior at lower and at higher energies is explained by the energy depth distributions shown in figures 5.7 and 5.8. At lower energies, the photon and the accompanying shower does not penetrate far inside the stack before interacting. Backscattering occurs and energy leaves the front end of the stack. It is seen that neither γ-rays with low energies nor their secondary particles have energy enough to pass to the last layers and therefore no energy is deposited beyond a depth of approximately 18 cm. At higher energies, the photon penetrates further before interacting and part of the shower may emerge from the opposite surface. For the highest energy, $E_{in} = 10240$ MeV, the first centimeter of the depth has the smallest energy deposition.

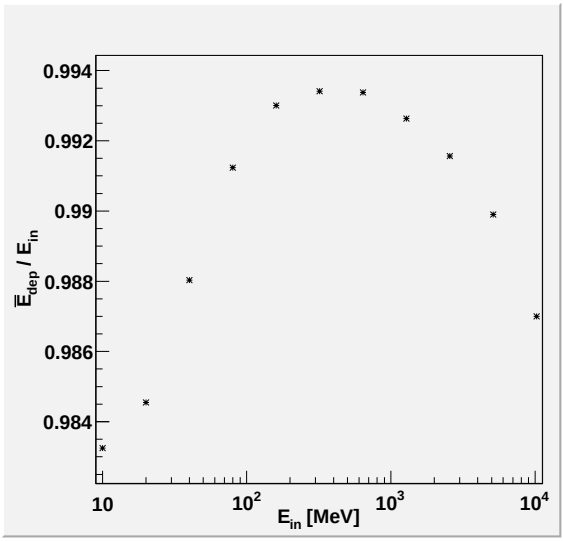

Figure 5.5: Mean energy deposition, $\bar{E}_{dep}$, for the whole stack as a function of incoming energy, E_{in}, in PWO. The particles with incoming energies around 500 MeV deposit maximum energy to the material. This simulation was done in Geant4.

A measure of the penetration of the particles is the mean free path, λ, which increases with energy. The average depth, $\bar{d}$, of the energy depth distributions in figures 5.7 and 5.8, as well as the corresponding standard deviation, σ_d, is shown in figure 5.6 as a function of energy. As expected, the values of both quantities increase with increasing energy (approximately linear as a function of the logarithm of the energy) in the high-energy range. One peculiar feature to notice, however, is the minimum at around 20 MeV.

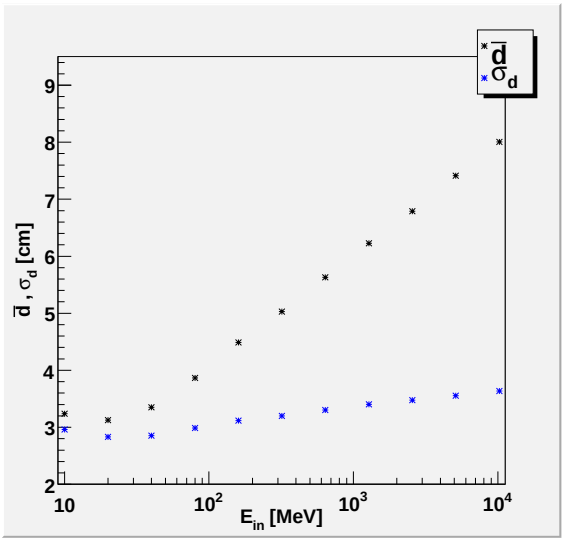

Figure 5.6: The mean value of the distance and the standard deviation, as a function of incoming energy.

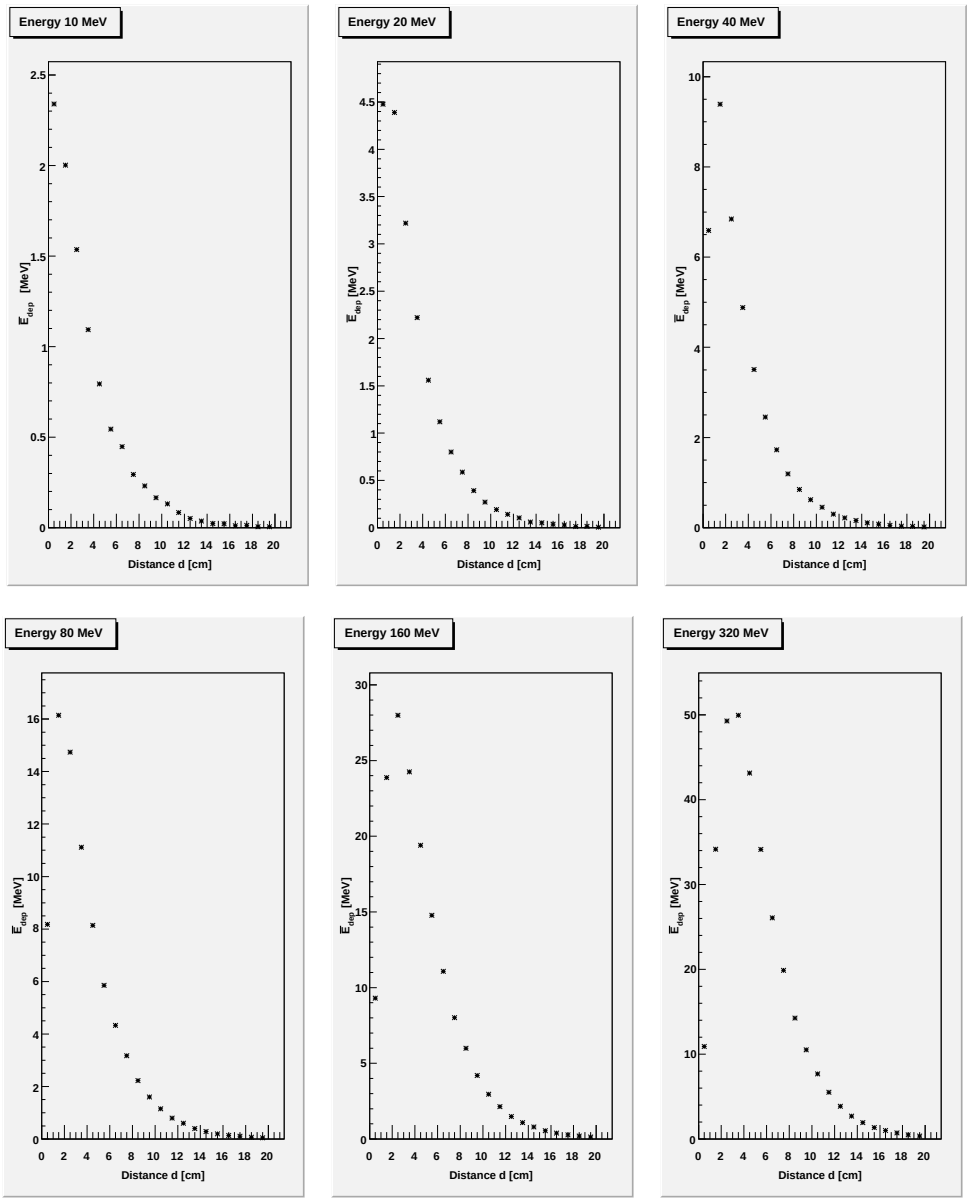

Figure 5.7: Energy deposited in 1 cm layer, $\bar{E}_{dep}$, for each layer of the PWO stack, as a function of distance d. The simulation was done in Geant4.

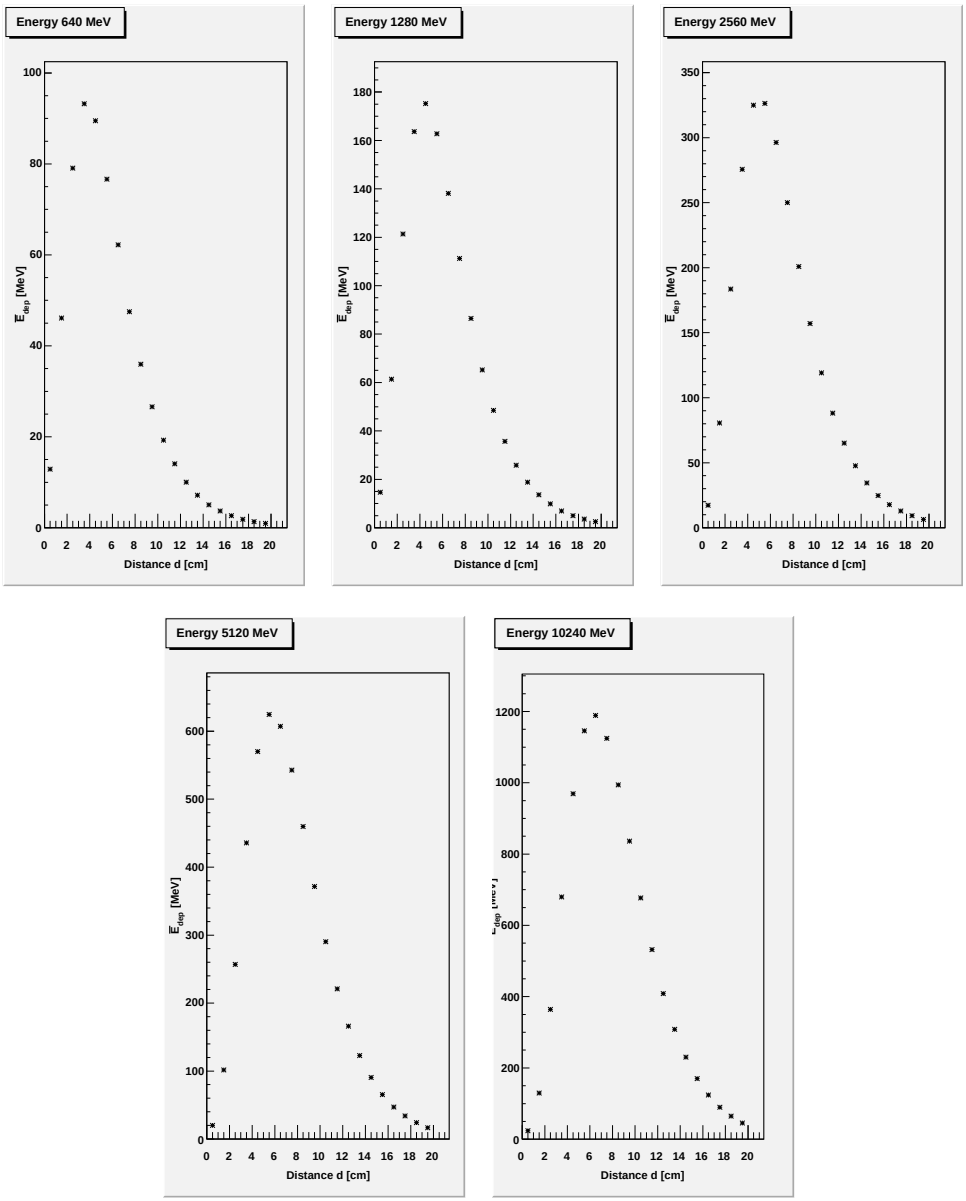

Figure 5.8: Energy deposited in 1 cm layer, $\bar{E}_{dep}$, for each layer or the PWO stack, as a function of distance d. The simulation was done in Geant4.

6 Contributions to the Energy Resolution

Three contributions to the energy resolutions are of concern in this thesis. These are the influence from the nonuniformity of the crystals, the energy leakage from the detector and the Poisson statistics of the light collection process in the scintillating material.

6.1 Energy leakage

The effect on the energy resolution due to energy leakage, $R_{\text{leak}} = \sigma_{\text{dep}}/\bar{E}_{\text{dep}}$, as a function of initial energy, E_{in}, is show in figure 6.1. Here σ_{dep} corresponds to the standard deviation of the deposit energy. For $E_{in} = 10$ MeV, this contribution is almost 5.7%. With E_{in} increasing, R_{leak} decreases and passes minimum at E_{in} is around 1500 MeV with R_{leak} approximately 0.9%. It then shows some indication of increasing again.

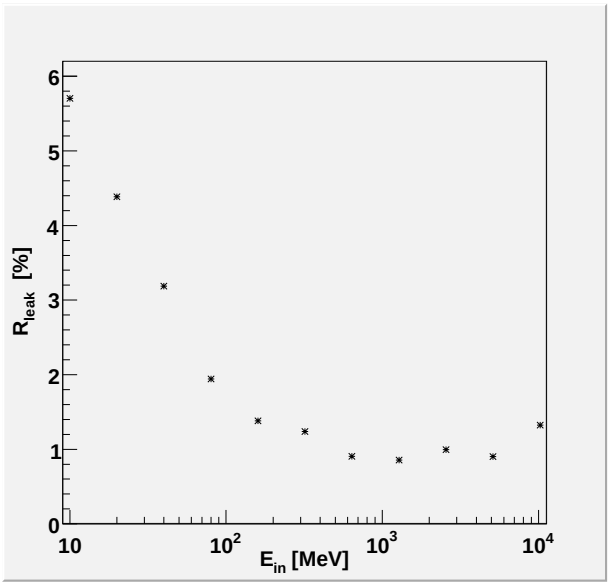

Figure 6.1: Energy dependence of the leakage energy resolution, R_{leak}, in PWO material. The simulation was done in Geant4.

6.2 Nonuniformity

In section 4.9 the light yield was measured for each of the eleven crystals. The variation in number of photoelectrons contribute to the energy resolution. To see how this nonuniformity may depend on the initial energy of the incoming γ-ray photon, E_{in}, the light yield results were folded with the energy depth distribution, E_{dep}, simulated in chapter 5.3.

The number of photoelectrons in event i, $n_{pe}(i)$, for each of the 10000 events, was calculated by

$$n_{pe}(i) = \sum_s E_s \beta_s \tag{6.1}$$

Here s is the layer number and E_s is the energy deposit in layer s. The measured light yield, β_m, was inter- and extrapolated to get the light yield in the middle of each layer, β_s.

The light yield for each event, $\beta(i)$, was then obtained by

$$\beta(i) = \frac{n_{pe}(i)}{\sum_s E_s} \tag{6.2}$$

Figures 6.2 and 6.3 show the energy dependence of the mean value of the light yield, $\bar{\beta}$, for each crystal. Since the incoming photon penetrates further inside the crystals for higher energies, E_{in}, the mean value of β should decrease, as can be seen in figures 4.12 and 4.13. This is almost the case, however, the light yield for $E_{in} = 10$ MeV is lower than for $E_{in} = 20$ MeV, for all crystals. This is in a consistent with the result for the mean value of distance, $\bar{d}$, (section 5.3).

The mean light yield is also very dependent on the tapering of the crystals. Figures 6.2 and 6.3 are plotted with intervals of same size, to make the comparison of $\bar{\beta}$ straightforward. The mean value of the light yield decreases approximately 8% for Crystal of Type 2 while Crystal of Type 11 decreases only around 3%, between 10 MeV and 10 GeV.

The relative standard deviation of the light yield, $R_\beta = \sigma_\beta/\bar{\beta}$, was calculated for each γ-ray photon energy, see figures 6.4 and 6.5. For every crystal, the largest contribution to the resolution appears at the lowest energy, $E_{in} = 10$ MeV and then decreases with increasing energy. For crystal of Type 2, the resolution due to nonuniformity is affected the most of all crystals. It has the largest contribution of approximately $R_\beta = 4.4\%$ and then falls to around $R_\beta = 1.9\%$ for the highest energy.

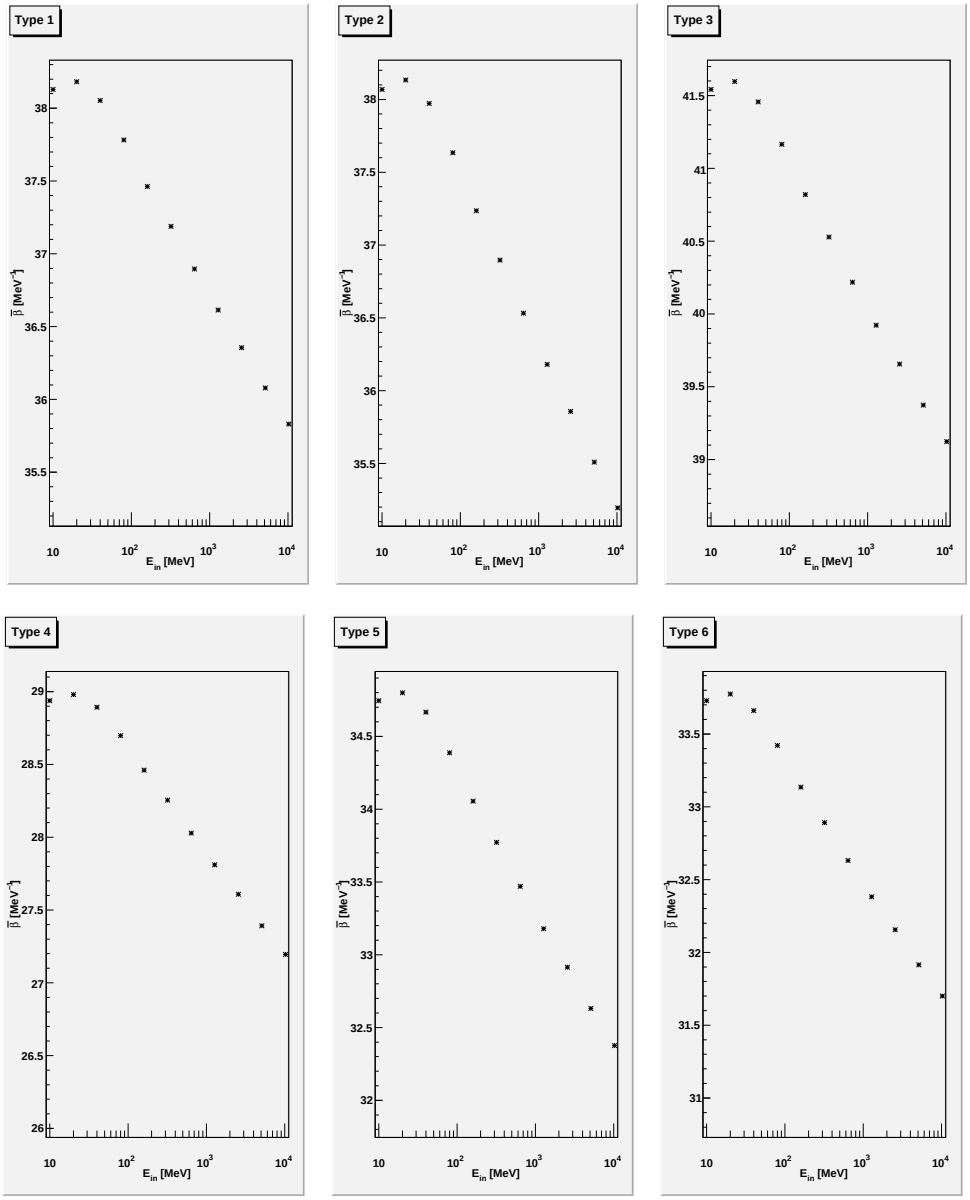

Figure 6.2: Mean number of the light yield, $\bar{\beta} = N_{pe}/E_{dep}$, as a function of energy E_{in}. The figures are plotted with intervals of same size, to make the comparison of $\bar{\beta}$ straightforward. Crystals of type 1 - 6.

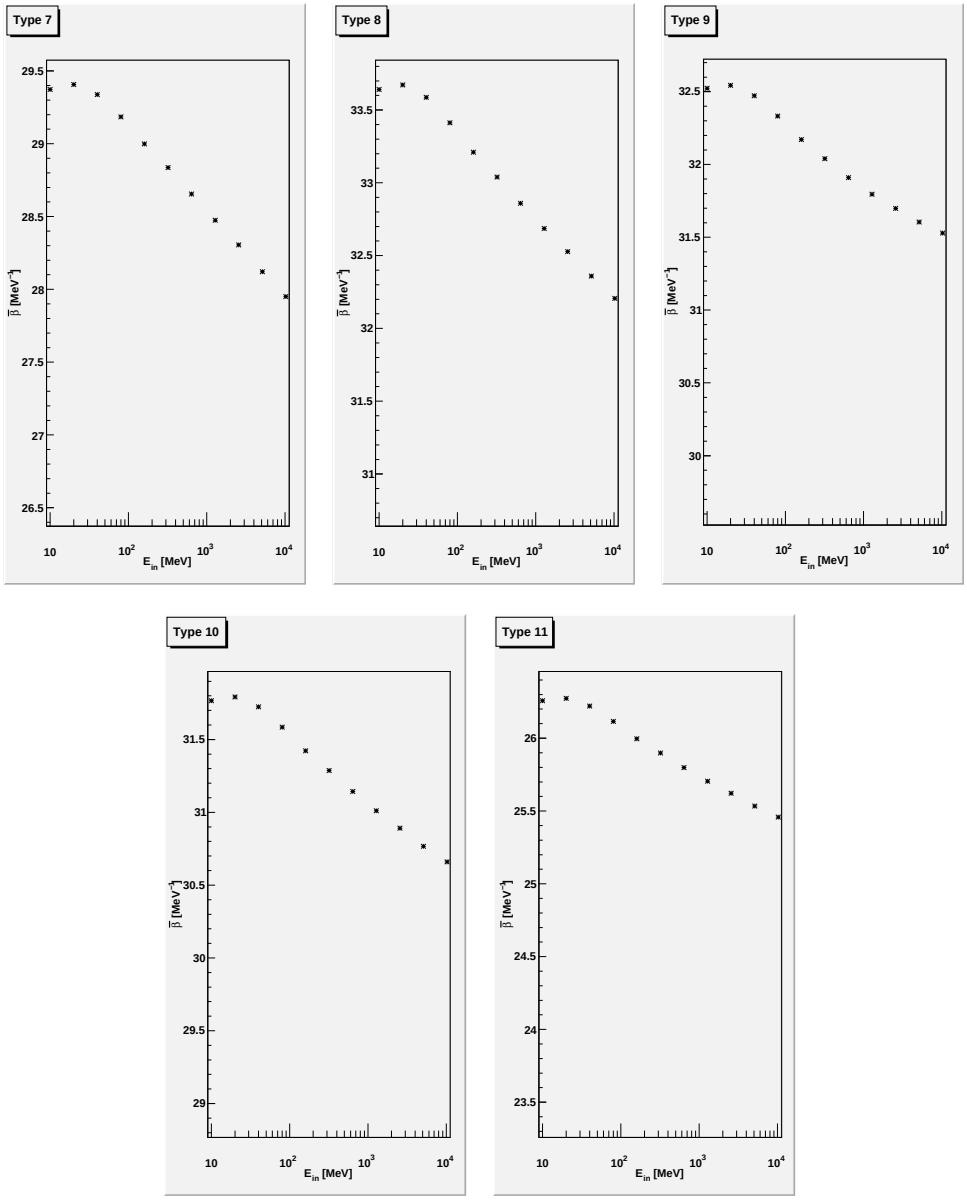

Figure 6.3: Mean number of the light yield, $\bar{\beta} = N_{pe}/E_{dep}$, as a function of energy E_{in}. The figures are plotted with intervals of same size, to make the comparison of $\bar{\beta}$ straightforward. Crystals of type 7 - 11.

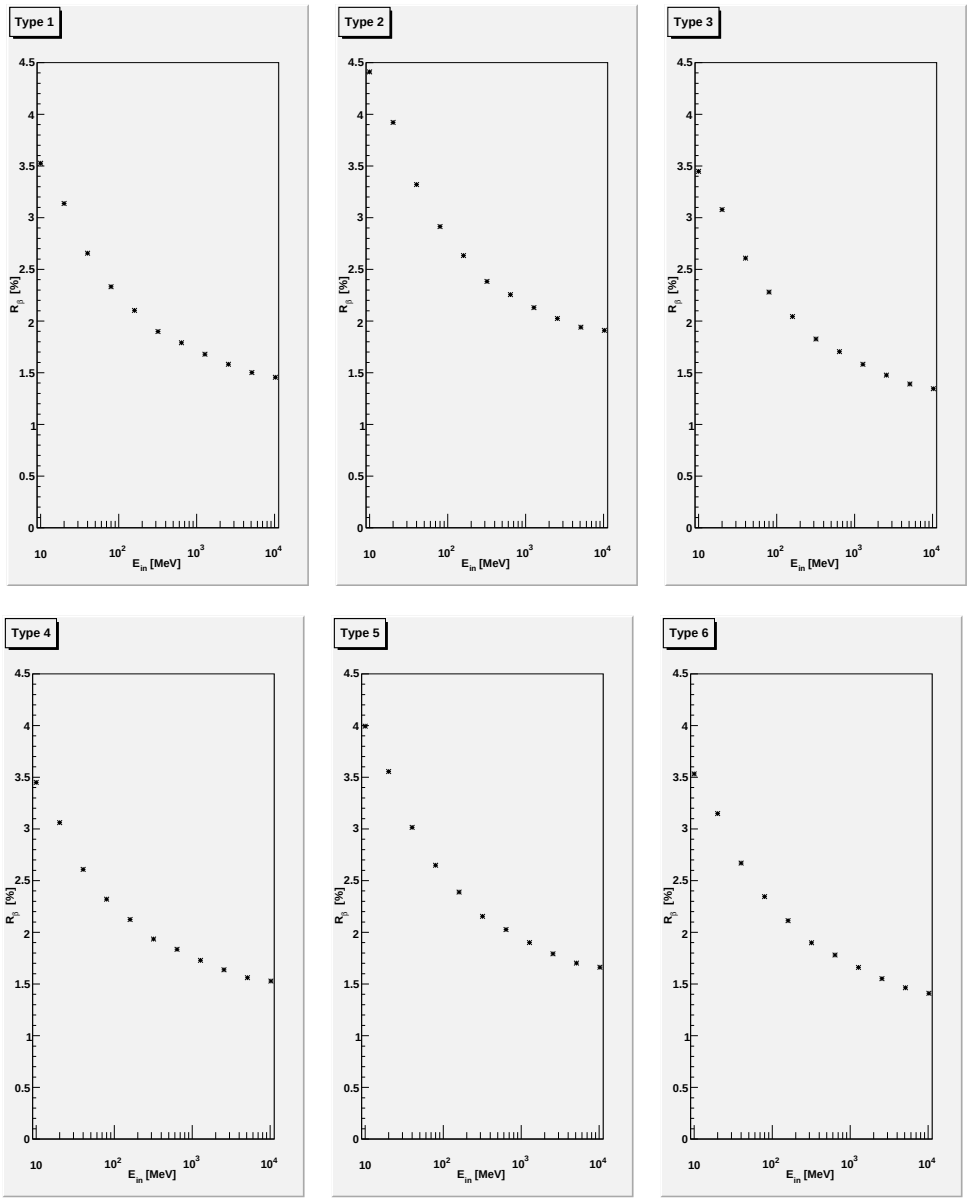

Figure 6.4: The relative standard deviation of the light yield, $R_\beta = \sigma_\beta/\bar{\beta}$, as a function of incoming energy E_{in}. Crystals of type 1 - 6.

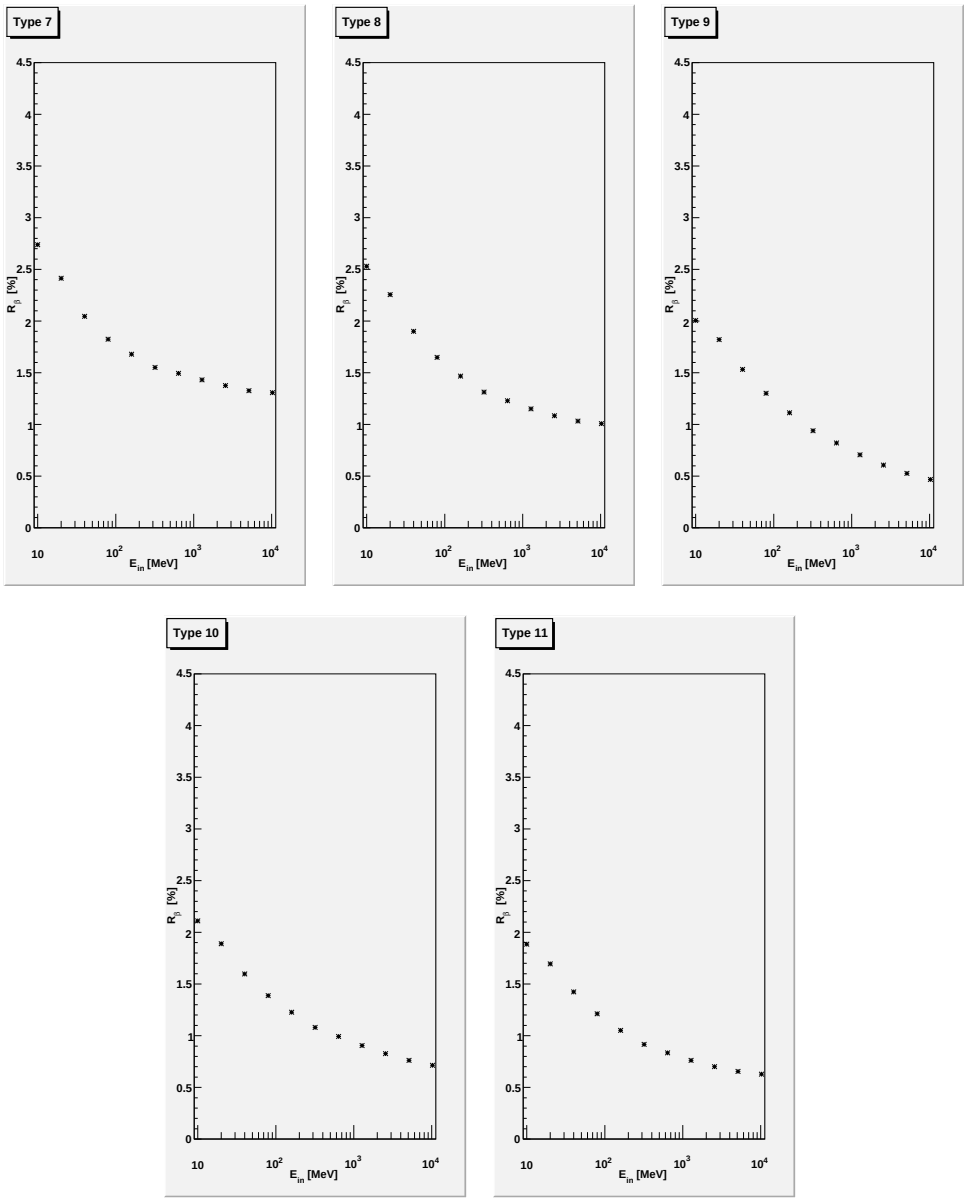

Figure 6.5: The relative standard deviation of the light yield, $R_\beta = \sigma_\beta/\bar{\beta}$, as a function of incoming energy E_{in}. Crystals of type 7 - 11.

6.3 Poisson statistics

In section 4.5 it was assumed that the number of secondary electrons in the photomultiplier tube follows a Poisson distribution. Therefore, from equation (4.5), the relative standard deviation for the number of photoelectrons, N_{pe}, hitting the first dynode, is

$$R_{\text{Poiss}} = \left(\frac{\sigma_{N_{pe}}}{\bar{N}_{pe}}\right) = \frac{1}{\sqrt{N_{pe}}} = \frac{1}{\sqrt{\beta E}} \tag{6.3}$$

As can be seen, the relative energy resolution worsen as the number of photoelectrons is reduces.

6.4 Comparison - Type 2 and Type 11

The energy resolution is influenced by the nonuniformity of the crystals, the energy leakage and Poisson statistics. These contributions are compared for crystal of Type 2 and Type 11, which have the largest and smallest tapering in shape respectively, see table 6.1.

The average light yield in the Poisson statistics was chosen to be $\beta = 25$ MeV^{-1}. This is a reasonable average value in the final PANDA calorimeter. The light yield in section 4.9 was not measured at $T = -25$°C and measured with photomultiplier tube which will not be used at PANDA.

Table 6.1: Contributions to the energy resolution for crystal of Type 2 and Type 11. The influences from nonuniformity, R_β, energy leakage, R_{leak}, and from Poisson statistics, R_{Poiss} for different γ-ray energies, E_{in}.

E_{in} [MeV]	R_{Poiss} [%]	R_{leak} [%]	Type 2, R_β [%]	Type 11, R_β [%]
10	6.3	5.7	4.4	1.9
10^2	2.0	1.8	2.8	1.1
10^3	0.6	0.9	2.2	0.8
10^4	0.2	1.3	0.9	0.7

For low energies, around 10 MeV, the Poisson statistics contributes the most to the resolution compared to other influences. It then decreases rapidly with energy and other influences contribute more. At the highest energies, the largest contribution comes from energy leakage. However, at the energy region in between, the nonuniformity of Type 2 has the largest influence. On the other hand, the crystal of Type 11, which was very little tapered in shape, the nonuniformity does not give a major contribution to the energy resolution.

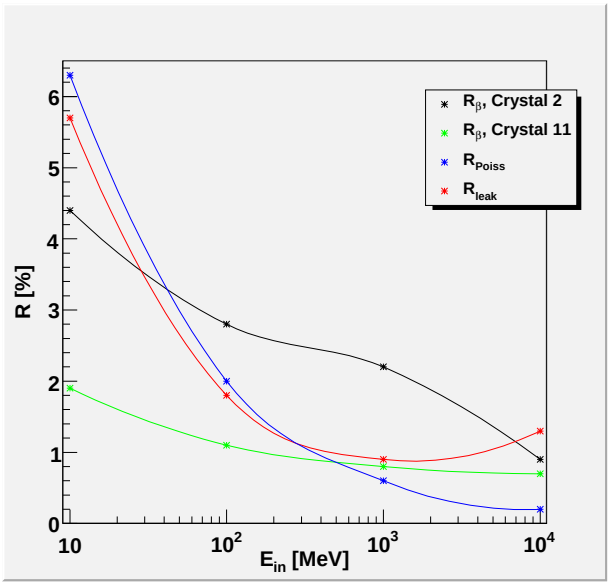

Figure 6.6: Contributions to the energy resolution for crystals of Type 2 and 11. The lines between the points are to guide the eye.

7 Conclusion

The light yield nonuniformity was measured for eleven scintillating crystals made of lead tungstate, PWO. These crystals are of different shapes which lead to variation in the results. The average value as well as the nonuniformity differed by approximately 30% and 70%, respectively, for different types of crystals. The nonuniformity is largest for crystals having largest tapering angles.

The nonuniformity results were corrected for varying temperatures along the crystals of the order of 0.5°C. The cnage of the light yield as a function of temperature was measured. A change of -1°C increased the light yield of 2.2%. This is in a consistance to other measurements [7].

The optical grease connecting the crystals and the PM tube as well as the wrapping around the crystals contribute to variations in the measured light yield. The nonuniformity and the mean value changed by 20% due to these effects between two measurements on a crystal of Type 1.

Simulations of γ-rays interacting with a stack of 20 PWO layers, each of thickness 1 cm, was done with Geant4. Lateral leakage was avoided. The energy deposit in each layer gave the energy depth distribution in the stack. As expected, the penetration of the photon and accompanying shower increased with energy.

Three contributions to the energy resolution were investigated. These are energy leakage from the detector, Poisson statistics of the light collection process and the measured nonuniformity of the eleven crystals. At the highest energies, the energy leakage has the largest contribution, for low energies the Poisson statistics influences the resolution the most. This is independent of the crystal type. To answer the question if the fluctuations in the measured light yield contributes to the energy resolution in such matter that it has to be compensated for, the measured light yield was folded with the energy depth distribution from the simulation. For crystals that are very tapered in shape, such as crystal of Type 2, the nonuniformity of the light yield has a major influence on the energy resolution for energies in the intermediate region. However, crystals with small tapering angles, such as the crystal of Type 11, this contribution is considerably smaller.

This first analysis of the eleven crystals located in the barrel of the electromagnetic calorimeter in PANDA shows that the light yield nonuniformity of crystals that are very tapered in shape do contribute significantly to the energy resolution for energies between 50 MeV to 7000 MeV. However, more measurements need to be done for all the crystals. It is not known for example how the crystals of the same type vary among themselves. Also, for each crystal, the measurement was done only once.

References

[1] The Panda Collaboration, *Technical Design Report for PANDA. Electromagnetic Calorimeter (EMC). Strong Interaction Studies with Antiprotons.* FAIR/GSI. August 2009.
`http://www-panda.gsi.de/archive/public/panda_tpr_EMC.pdf`

[2] S. Grape, *PWO Crystals Measurements and Simulation Studies of $\bar{\Lambda}$ Hyperon Polarisation for PANDA.* Licenciate Thesis at Uppsala University. January 2008.

[3] The homepage of KVI-GSI Programme at FAIR. August 2009.
`http://www.kvi.nl/fair/research/panda.html`

[4] The homepage of Panda-GSI. August 2009.
`http://www-panda.gsi.de/html/det/emc/emc.htm`

[5] G. F. Knoll, *Radiation Detection and Measurement - third edition.* John Wiley & Sons, Inc. New York. 2000.

[6] W. R. Leo, *Techniques for Nuclear and Particle Physics Experiments.* Springer-Verlag, Berlin Heidelberg. 1994.

[7] The Panda Collaboration. *Technical Process Report for PANDA. Strong Interaction Studies with Antiprotons.* FAIR/GSI. August 2009.
`http://www-panda.gsi.de/archive/public/panda_tpr.pdf`

[8] The homepage of sales department for Hamamatsu Photomultiplier Tube. August 2009.
http://sales.hamamatsu.com/assets/pdf/parts_R/R2083.pdf

[9] S. Grape, *Studies of PWO Crystals and Simulations of the $\bar{p}p \rightarrow \bar{\Lambda}\Lambda, \bar{\Lambda}\sum^0$ Reactions for the PANDA Experiments.* Doctor Thesis at Uppsala University. To be published.

[10] The homepage of Geant4. July 2009.
`http://geant4.web.cern.ch/geant4/geant4_public/source/geant4/examples/novice/N03/README`